Brief communication

Pooling signals from vertically and non-vertically orientation-tuned disparity mechanisms in human stereopsis

Saumil S. Patel [a,b,c,*], Harold E. Bedell [b,c], Preetha Sampat [b]

[a] *College of Engineering, University of Houston, Houston, TX 77204-4005, USA*
[b] *College of Optometry, University of Houston, Houston, TX 77204-4005, USA*
[c] *Center for Neuro-Engineering and Cognitive Science, University of Houston, Houston, TX 77204-4005, USA*

Abstract

To understand the role that orientation-tuned disparity-sensitive mechanisms play in the perception of stereoscopic depth, we measured stereothresholds using two sets of random-dot stimuli that produce identical stimulation of disparity mechanisms tuned to vertical orientation but dissimilar stimulation of disparity mechanisms tuned to non-vertical orientations. Either 1 or 1.5 D of astigmatic blur was simulated in the random-dot images presented to both eyes, using two axis configurations. In the parallel-axis conditions, the axis of simulated astigmatic blur was same in the two eyes (0, 45 or 135 o[rientation] deg). In the orthogonal-axis conditions, the axes of astigmatic blur were orthogonal in the two eyes (LE: 180, RE: 90; LE: 90, RE: 180; LE: 45, RE: 135; and LE: 135, RE: 45). Whereas the stimulation of disparity mechanisms tuned to near-vertical orientations should be similar in the oblique parallel- and orthogonal-axis conditions, the stimulation of non-vertically tuned disparity mechanisms should be dissimilar. Measured stereothresholds were higher in the orthogonal compared to the parallel-axis condition by factors of approximately 2 and 5, for 1 and 1.5 D of simulated oblique astigmatic blur, respectively. Further, for comparable magnitudes of simulated astigmatic blur, stereothresholds in the (LE: 180, RE: 90 and LE: 90, RE: 180) conditions were similar to those in the (LE: 45, RE: 135 and LE: 135, RE: 45) conditions. These results suggest that the computation of horizontal disparity includes substantial contributions from disparity mechanisms tuned to non-vertical orientations. Simulations using a modified version of a disparity-energy model [Qian, N., & Zhu, Y. (1997). Physiological computation of binocular disparity. *Vision Research, 37,* 1811–1827], show (1) that pooling across disparity mechanisms tuned to vertical and non-vertical orientations is required to account for our data and (2) that this pooling can provide the spatial resolution needed to encode spatially changing horizontal disparities.
© 2005 Elsevier Ltd. All rights reserved.

Keywords: Stereoscopic depth perception; Orientation tuning; Energy model; Oblique disparity

1. Introduction

The slightly different views of the visual world that are registered in the two eyes are combined in the brain to create a three dimensional percept (Wheatstone, 1838). The common belief is that cortical neurons tuned to vertical orientation are largely responsible for encoding horizontal disparities in the two views and hence the perception of stereoscopic depth. However, a large number of neurons are found in visual cortical areas that are sensitive to disparities between stimuli with non-vertical orientations (Anzai, Ohzawa, & Freeman, 1997; Barlow, Blakemore, & Pettigrew, 1967; Chino, Smith, Hatta, & Cheng, 1997; Felleman & Van Essen, 1987; Gonzalez, Krause, Perez, Alonso, & Acuna, 1993; Hubel & Wiesel, 1970; Maske, Yamane, & Bishop, 1986; Maunsell & Van Essen, 1983; Ohzawa, DeAngelis, & Freeman, 1990; Poggio, Motter, Squatrito, & Trotter, 1985; Prince,

---

* Corresponding author. Tel.: +1 713 743 1995; fax: +1 713 743 2053.

E-mail address: saumil@swbell.net (S.S. Patel).

Pointon, Cumming, & Parker, 2002; Smith et al., 1997). It is not known what role, if any, this large number of neurons tuned to non-vertical orientations play in stereovision.

When a horizontal position disparity is introduced in a broad-band binocular stimulus, phase disparities arise at all orientations (shown in the Fourier phase disparity matrix in Fig. 1A). Phase disparity is defined as the dif-
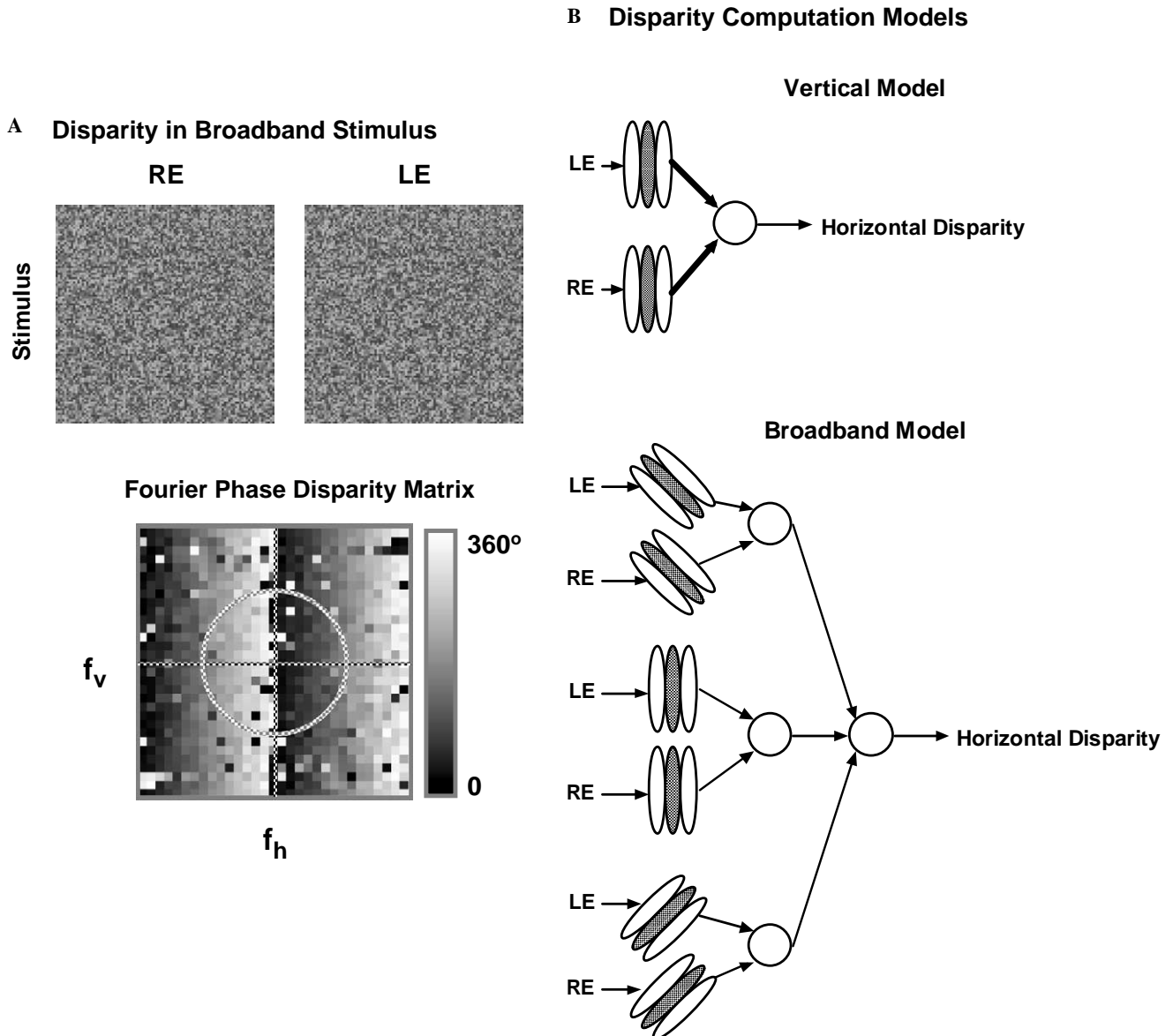

Fig. 1. (A) Distribution of phase disparities for a broad-band random-dot stimulus containing horizontal position disparity. The images for each eye are shown in the top half of the figure. Each eye's image consists of a 100×100 pixel outer frame and a 31×31 pixel central square. The dots in the outer frame are correlated. Horizontal disparity is created in the stimulus by shifting the central square in the right eye's image leftward relative to the left eye's image by two pixels. If the images are cross-fused, a central square will be perceived in front of the outer frame. The phase disparities at various orientations and SFs are computed by first transforming each eye's central 31×31 pixel sub-image to the Fourier domain. The phase disparity matrix is computed as the difference between the spatial phase matrix of the sub-images of the two eyes. A coordinate system is defined within the phase disparity matrix by the vertical and horizontal lines. The origin of the coordinate system corresponds to the DC component. The horizontal (vertical) line in the phase disparity matrix represents vertically (horizontally) oriented SF components. All other elements in the matrix represent oriented SF components, whose vertical and horizontal luminance modulation components are given by projections on to the vertical axis (f_v) and horizontal axis (f_h), respectively. Note that this decomposition of luminance modulation in oriented SF components is largely mathematical. Based on the fact that neurons that process disparities from oriented SF components are orientation tuned, it is more appropriate to treat these SF components and the disparities they carry as unitary quantities, i.e., as oblique SF components and *oblique phase disparities*, respectively. The locus of points on the circle in the phase disparity matrix represents a set of Fourier components having the same SF. (B) Representation of the vertical and broad-band models of horizontal disparity computation. In the vertical model, only the neurons tuned to vertical orientations in the stimulus are used to compute horizontal image disparity. In the broad-band model, non-vertical as well as vertically tuned neurons contribute.

ference between the spatial phases of a spatial frequency (SF) component in the images seen by the two eyes. The spatial phase is defined as the position shift of a single SF grating (with respect to an arbitrary reference, for example, center of the stimulus) along the direction of maximum luminance modulation, expressed in angular units. For a given spatial frequency (e.g., the points on the circle in the Fourier matrix in Fig. 1A), the phase disparity is largest in the vertical orientation, which is represented on the horizontal axis of the matrix. As the orientation of the SF component changes from vertical to horizontal, the phase disparity decreases toward zero according to a cosine function. Consequently, if we assume that the level of phase disparity noise is similar in all disparity-tuned neurons, then the disparity neurons tuned to near-vertical orientations should have the highest signal-to-noise ratio for phase disparity for each preferred SF. It is therefore possible that the stereovision system processes disparity information using only the most sensitive (termed vertically-tuned hereafter) neurons, and entirely ignores the information from neurons tuned to non-vertical orientations.

Contrary to this possibility, previous psychophysical studies suggested that oblique disparities play a substantial role in perception of stereoscopic depth (Blake, Camisa, & Antoinetti, 1976; Farell, 1998; Mansfield & Parker, 1993; Morgan & Castet, 1997; Patel et al., 2003b; Simmons & Kingdom, 1995; van Ee & Anderson, 2001). However, it is not clear what type of mechanisms processes the disparity information from oblique spatial frequency components in a broad-band stimulus, or what kind of processing is involved. Here, we provide clear psychophysical evidence that the disparity information from non-vertical orientations substantially improves the performance of the stereovision system. In particular, we present data that reject a disparity-computation model based solely on vertically tuned binocular cells (the vertical model) in favor of a model that is based on non-vertically as well as vertically tuned binocular cells (referred to hereafter as a broad-band model).

The logic of our experiments depends on the well established observation that stereoacuity, defined as the smallest horizontal disparity that produces a reliable perception of stereoscopic depth, is degraded if the contrast in the two monocular images is reduced, and is degraded even more so if the contrast in the monocular images is reduced unequally (Halpern & Blake, 1989; Hess, Liu, & Wang, 2003; Legge & Gu, 1989; Schor & Heckmann, 1989; Simons, 1984; Stevenson & Cormack, 2000; Westheimer & McKee, 1980; Wood, 1983). The additional degradation of stereoacuity when the contrast of the monocular images is unequal is a consequence of a mismatch between the two monocular signals. By spatially filtering each monocular image separately, it is possible to create mismatches between the contrast of specific spatial frequency (SF) components in the two images. We used this strategy to evaluate the role of oblique disparities in the perception of stereoscopic depth, by comparing the stereothresholds for filtered random-dot stimuli that included inter-ocular mismatches between the contrast of oblique SF components to those for similar stimuli with the same contrast in each eye's image for all SF components.

The random-dot stimuli were spatially filtered in an orientation- and SF-dependent manner. A key feature of the spatial filter used for each eye's image was that it was designed to attenuate the contrast of SF components in an orientation-dependant manner (see Fig. 2A). In each monocular image, contrast attenuation was maximal for SF components oriented parallel to a specific angle, which is defined as increasing from 0 to 180 in the counter-clockwise direction with respect to the physical horizontal. This angle is called the axis of the filter and the filter simulates blurring induced by a plus-power cylindrical lens with the same axis. For SF components oriented at off-axis angles, the contrast attenuation decreased as the angular difference from the filter axis increased. Minimum contrast attenuation occurred for SF components oriented orthogonally to the axis of the filter. For one set of stimuli, the axis of the filter was 45 o(orientation)deg in the left eye and 135 odeg in the right eye (i.e., 45, 135), or vice-versa. For the second set of stimuli, the axis of the filter was either 45 odeg or 135 odeg in both eyes. We call the experimental condition that used the first set of stimuli the orthogonal-axis condition and the condition that used the second set of stimuli the parallel-axis condition. Sample stimuli from our experiments are shown in Fig. 2B. The main point to notice is that the stimuli in both the orthogonal- and parallel-axis conditions provide identical inter-ocular contrast to disparity-detecting mechanisms that are tuned to the vertical orientation (termed vertically tuned disparity-detecting mechanism hereafter). Consequently, if the sensitivity of the stereovision system is determined solely by mechanisms tuned to near-vertical orientations (vertical model) then compared to a condition with no filtering, the reduction in stereoacuity should be similar in the orthogonal- and parallel-axis conditions. On the other hand, the inter-ocular contrast in the orthogonal-axis condition is mismatched for the SF components at nearly every orientation. The largest mismatch of inter-ocular contrast occurs in this condition for SF components at 45 and 135 odeg, whereas an equal reduction of contrast in each eye's image occurs only for horizontal and vertical SF components. Therefore, if the sensitivity of the stereovision system depends also on mechanisms tuned to non-vertical orientations (broad-band model) then a greater reduction of stereoacuity is predicted in the orthogonal- compared to the parallel-axis condition.
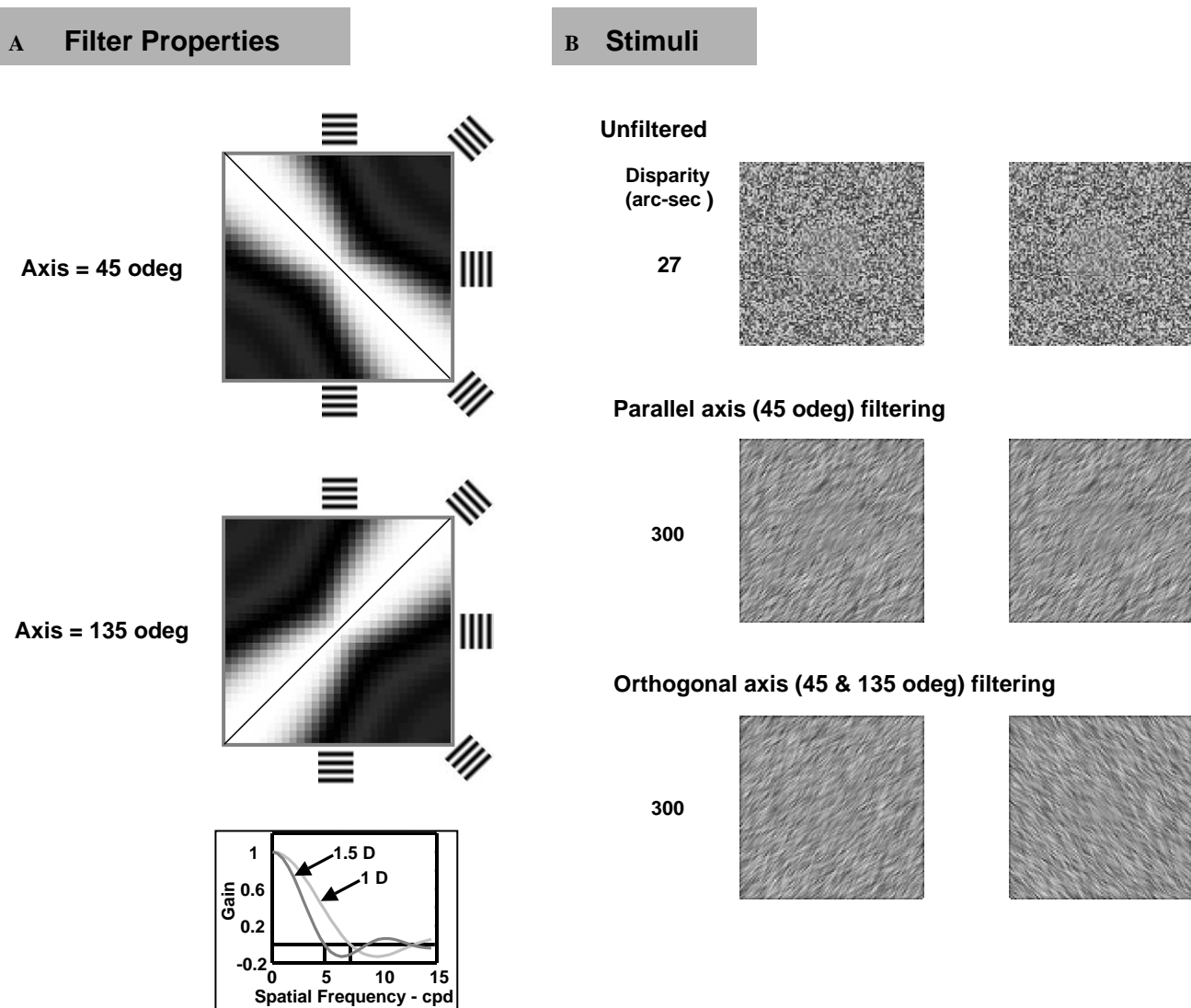
Fig. 2. (A) Illustration of the properties of the spatial filters used in our experiments. The top and middle panels depict the gains of sample filters (axis = 45 and axis = 135) as a function of the orientation angle and SF of the Fourier components. The panels depict the Fourier amplitude matrices of the filters. The Fourier components on a vertical line that passes through the center of the Fourier matrix are arbitrarily assigned the within-matrix reference orientation of zero and represent SF components that are oriented horizontally. The orientation angle of SF components increases in the clockwise direction and reaches 90 odeg (or vertical) on an imaginary horizontal line that passes through the center of the Fourier matrix. Examples of the physical orientations of SF components for several within-matrix orientations are depicted by the cartoons that surround each matrix. The axis of the filter in the top and middle panel is indicated by a black line. The gray shading in the top and middle panels indicates the contrast gain produced by the filter for SF components at various orientations, with black and white representing zero and maximum gain, respectively. In other words, for the filter depicted in the top (middle) square, gain is a minimum for SF components oriented at within-matrix 45 (135) odeg, i.e., for SF components oriented parallel to the axis of the filter. For off-axis SF components, contrast attenuation decreases as the orientation angle with respect to the axis increases. Filter gain as a function of SF (for the orientation parallel to the filter axis) is shown in the bottom panel for 1 and 1.5 D of simulated astigmatic blur. (B) Examples of the random-dot stimuli used in our experiments. Note that electronic conversion of file formats may have spatially distorted these images. No distortion was present in images used for our experiments. Each image within a pair is presented to just one eye. The images in the top row are unfiltered, and those in the middle and bottom rows are filtered to simulate an astigmatic blur of 1.5 D. The filter axes are the same for the images presented to each eye in the middle row, and are orthogonal for the images in the bottom row. Each monocular image contains an inner and an outer frame. The imaginary outline of the inner square and all of the random-dots in the outer frame are at zero disparity. Phase disparities that are consistent with a specific horizontal position disparity are introduced in all SF components of the inner squares presented to each eye. If the reader cross-fuses the images, the inner square should be perceived in front of the outer frame in each of the top two pairs. The values of horizontal position disparity shown at the left of each image pair are correct if the figure is viewed from a distance where each outer frame subtends 3.3 deg.

2. Methods

2.1. Procedure

Observers ($N = 3$, all authors but one of the authors at the time of data collection was naïve about the purpose of the experiments) fused a pair of random-dot (RD) images, presented separately to each eye on the left and right sides of a Macintosh computer monitor, using pairs of orthogonal polarizers. Each eye's unfiltered image consisted of a 1-deg (31×31 pixels) inner square of RDs centered in a 3.3-deg (100×100 pixels) outer frame of RDs. The Michelson contrast for the inner square and the outer frame in the unfiltered images was 50%. The background and mean luminance of the random-dot stimuli, after accounting for attenuation by the polarizers placed in front of the screen and on the eyes, were 0.12 and 3.1 cd/sq-m, respectively. The outer frames in the two images provided a reference plane for the disparities that were introduced in the inner square. The outline of the two inner squares remained fixed at zero disparity and coherent position disparities were produced within the two inner squares by manipulating each image's Fourier phase spectrum. The amplitude spectrum of each eye's unfiltered image was identical. Stereothresholds were measured for stimulus conditions that varied according to the spatial filter used for each eye's image. For each set of conditions, the monocular images were spatially filtered to simulate 1.0 and 1.5 D of astigmatic blur with a pupil diameter of 3.5 mm (for details see below). The gains of the 1 and 1.5 D filters for spatial frequencies parallel to the filter axis are shown as a function of spatial frequency in Fig. 2A (bottom left). The principal cut-off (i.e., first zero crossing) frequencies that correspond to 1 and 1.5 D of astigmatic blur are 7 and 4.6 cpd, respectively. Experimental conditions were grouped based on whether the axis of the filter (or, the axis of astigmatic blur) was the same (parallel condition) or orthogonal (orthogonal condition) in the two eyes. The filter axes used were 45, 90 (vertical), 135, and 180 (horizontal) o[rientation]deg. The gains of sample filters, with 135 and 45 odeg axes, as a function of orientation, are illustrated in Fig. 2A (left top and middle). On each trial, the observer used a joystick to indicate whether the inner square was in front or behind the outer frame. The stimulus remained on the screen until the observer responded. From trial to trial, the disparity in the inner square varied randomly according to the method of constant stimuli and stereothresholds were defined as the inverse slope (50–84%) of the resulting psychometric function. Stereothresholds were measured for each condition and observer at least twice.

2.2. Spatial filtering

The orientation-dependant spatial filtering of each eye's image was achieved by simulating astigmatic blur,

created by modifying a technique used previously to simulate spherical blur (Akutsu, Bedell, & Patel, 2000). All image manipulations were performed in Matlab. Image blur was produced after introducing the appropriate disparities between the two monocular images. The filter for a given magnitude and axis of astigmatic blur was designed in the Fourier domain. The size of the Fourier matrix was the same as the size of each eye's image, i.e., 100×100 elements. The imaginary component of each element in the Fourier matrix was set to zero. Each real element of the Fourier matrix $A(i,j)$ was computed as follows:

$$A(i,j) = J_0(x_{ij}) + J_2(x_{ij}), \tag{1}$$

where, $J_n()$ is the nth order Bessel function and, i and j are the row and column indices of the selected Fourier component. The DC component is located at element $(51, 51)$ in the matrix. The argument of the Bessel functions, x_{ij}, is computed as follows:

$$x_{ij} = \pi\omega_{ij}pD\cos^2(\alpha - \theta_{ij}). \tag{2}$$

Here, ω_{ij} is the angular SF and is given by,

$$\omega_{ij} = \frac{f_{ij}}{0.0214} \tag{3}$$

where f_{ij} is the SF in cycles per degree that corresponds to the (i,j) matrix element. In Eq. (3), the SF, f_{ij} is given by:

$$f_{ij} = f_s\sqrt{(i - 51)^2 + (j - 51)^2}, \tag{4}$$

where f_s is the scale factor for conversion of discrete SF to SF in cycles per degree. Referring back to Eq. (2), p is the pupil diameter in meters, which was set to 0.0035. D is the magnitude of the astigmatic blur in Diopters and θ_{ij} is the within matrix orientation angle corresponding to the (i,j) matrix element with respect to the *vertical* line that passes through the DC component in the Fourier matrix. θ_{ij} is given by:

$$\theta_{ij} = \frac{\pi}{2} - \arctan((51 - i)/(j - 51)). \tag{5}$$

The case in which the denominator of Eq. (5) is zero was specially handled. Note that the Fourier component that represents a vertically oriented grating is assumed to lie on the horizontal line that passes through the DC component in the Fourier matrix and will have θ_{ij} equal to 90 odeg. This convention differs from that in our previous papers (Patel, Ukwade, Bedell, & Sampath, 2003a; Patel et al., 2003b), in which the within-matrix orientation angle of each SF component was defined with respect to the horizontal line passing through the DC component in the Fourier matrix. In Eq. (2), note that α is the axis of the astigmatic blur, which is defined with respect to the physical horizontal and is the same as the clinical axis of astigmatism. The Fourier matrix for the filter was inverse transformed to obtain a filter kernel.

Each monocular image was filtered in the image domain by convolving it with the appropriate kernel.

3. Results and discussion

3.1. Psychophysics

The observers fused the stimuli used in our experiments and did not report diplopia or binocular rivalry when asked after each session. However, we must acknowledge that the observers were not actively looking for binocular rivalry and its occasional occurrence could have largely gone unnoticed. The measured stereoacuity in the orthogonal- and parallel-axis conditions is shown for two experienced and one naïve observer in Fig. 3A (see caption for details). A repeated-measures ANOVA was used to analyze the data collected from the three observers. The ANOVA model was a full-interaction model with two main factors: axis configuration and blur amplitude. The levels of axis configuration were parallel (average of 45/45 and 135/135) and orthogonal (average of 45/135 and 135/45). The levels of blur amplitude were 1 and 1.5 D. Contrary to the pre-
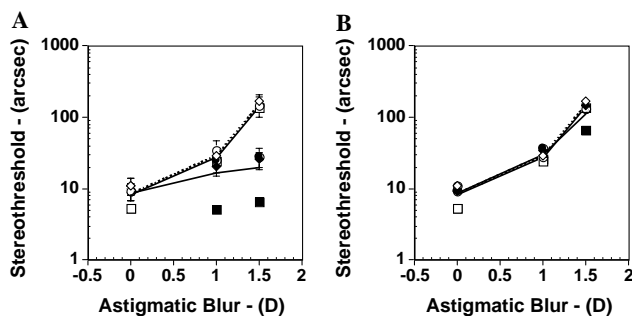

Fig. 3. (A) Stereothresholds are plotted as a function of the magnitude of astigmatic blur in the oblique orthogonal- and parallel-axis conditions. The axis of astigmatic blur in the orthogonal-axis condition was 45 odeg in one eye and 135 odeg in the other eye. The data shown for each observer (unfilled symbols) are the average of the (45,135) and (135,45) conditions. The dotted line in this as well as (B) indicates the stereothresholds in the orthogonal-axis condition averaged across all the observers. The axis of astigmatic blur in the parallel axis condition was 45 or 135 deg in both eyes. The data shown for each observer (filled symbols) are the average of the (45,45) and (135,135) conditions. Error bars represent the standard error within each observer. The solid line in (A) and (B) represents the stereothresholds in the parallel-axis condition averaged across all of the observers. The elevation of stereothresholds for 1.5 D of simulated astigmatic blur is substantially greater in the orthogonal-axis condition compared to the parallel-axis condition. (B) Stereothresholds are shown as a function of the magnitude of astigmatic blur in the (45,135) and (90,180) orthogonal-axis conditions. The data for the (45,135) condition (unfilled symbols) are replotted from panel (A). The data shown for each observer in the (90,180) condition (filled symbols) are the average of the (90,180) and (180,90) conditions. The elevation of stereothresholds in the (90,180) orthogonal-axis condition is virtually identical to that in the (45,135) condition.

diction of the vertical model and consistent with that of the broad-band model, stereoacuity is degraded substantially more in the orthogonal- than the parallel-axis condition ($F[1,2] = 339$, $p = 0.003$). The larger difference in our data for orthogonal vs. parallel axes at 1.5 D compared to 1 D are consistent with the findings of Cormack, Stevenson, and Landers (1997).

We next compared stereoacuity in an orthogonal-axis condition in which the filter axes were 90 and 180 odeg to the results obtained with orthogonal filter axes that were oblique. The orthogonal-axis condition (90, 180) produced a maximum mismatch between the contrast of the vertical and horizontal SF components presented to each eye, but offered equal inter-ocular contrast in the components at 45 and 135 odeg. By comparing the stereoacuities in the (90, 180) and the (45, 135) stimulus conditions, we can infer the relative contributions of disparity information from vertical vs. oblique SF components to the perception of stereoscopic depth. In particular, if most of the information about binocular disparity were carried by vertical and near-vertical SF components, then we would expect stereoacuity to be degraded substantially more in the (90, 180) compared to the (45, 135) orthogonal-axis condition. In addition, both of these orthogonal-axes conditions would be expected to produce similar conditions for binocular rivalry. The results for the three observers were analyzed using a repeated-measures, full-interaction ANOVA model with two main factors: axis configuration and blur amplitude. The levels of axis configuration were 45/135 and 90/180. The levels of blur amplitude were 1 and 1.5 D. In agreement with the broad-band model and previous suggestions that binocular matching is not limited to the horizontal direction (Farell, 1998; Morgan & Castet, 1997; Stevenson & Schor, 1997) the degradation of stereoacuity is similar in the (90,180) and (45,135) orthogonal-axis conditions (Fig. 3B; $F[1,2] = 5.5$, $p = 0.14$).

Although additional parallel-axis conditions of (90, 90) and (180, 180) were also run, these data do not provide additional information regarding the main conclusions drawn in this paper. The average stereothresholds in the (90,90) and (180,180) parallel-axis control conditions for 1 D (1.5 D) of astigmatic blur were 19 (34) and 11 (20) arc sec, respectively, and are reported here only for the sake of completeness. The lower thresholds in (180,180) conditions compared to (90,90) conditions are consistent with the hypothesis that disparity mechanisms tuned to vertical orientations have the highest signal-to-noise ratio within the stereovision system. The presence of hyperacuity level stereopsis in the (90,90) condition, in which contributions from disparity mechanisms tuned to near-vertical orientations are expected to be relatively less, illustrates consistency with the hypothesis that oblique disparities contribute substantially to stereopsis.

Previously, Chen, Hove, McCloskey, and Kaye (2005) measured stereoacuity for stimuli that were subjected to optical astigmatic blur at various axes. They also found that stereothresholds were substantially higher in their oblique orthogonal-axis (45, 135) condition compared to the vertical (90, 90) and horizontal (180, 180) parallel-axis conditions. However, they did not measure stereoacuity in the oblique parallel-axis condition. Also, the stimuli in their experiments did not contain contrast energy at all non-vertical orientations, which makes the contribution of oblique disparities to their results difficult to interpret. Finally, because they produced orientation-specific stimulus blur using cylindrical spectacle lenses instead of spatial filtering, they introduced meridional differences in image magnification that can degrade stereoacuity independently of image blur (Lovasik & Szymkiw, 1985).

3.2. Additional analyses and modeling

To illustrate how our results indicate the need for non-vertically oriented SF components in the computation of horizontal disparity, we performed horizontal cross-correlations between sample pairs of images that were used in the parallel and orthogonal axes conditions

in our experiments. For the images in each condition, cross-correlation was performed on images that were (a) filtered to contain only vertically oriented SF components, (b) filtered to contain a small ±15 deg band of oriented SF components around vertical, or (c) left unfiltered. The results of the cross-correlations are shown in Fig. 4; details of the analysis are provided in the figure caption. Whereas the disparity energy in our two sets of stimuli is similar in the vertically (Fig. 4A) and near-vertically (Fig. 4B) oriented spatial frequency components presented to the two eyes, the disparity energy differs substantially between these sets of stimuli when all of oriented spatial frequency components are considered (Fig. 4C). In particular, the horizontal inter-ocular correlation is substantially weaker for the unfiltered stimuli in the orthogonal-axis condition than in the parallel-axis condition. This analysis indicates that the large difference in stereo-sensitivity that we found in the parallel and orthogonal conditions of our experiments requires that the horizontal inter-ocular correlation be computed from non-vertically as well as vertically oriented SF components in the stimulus.

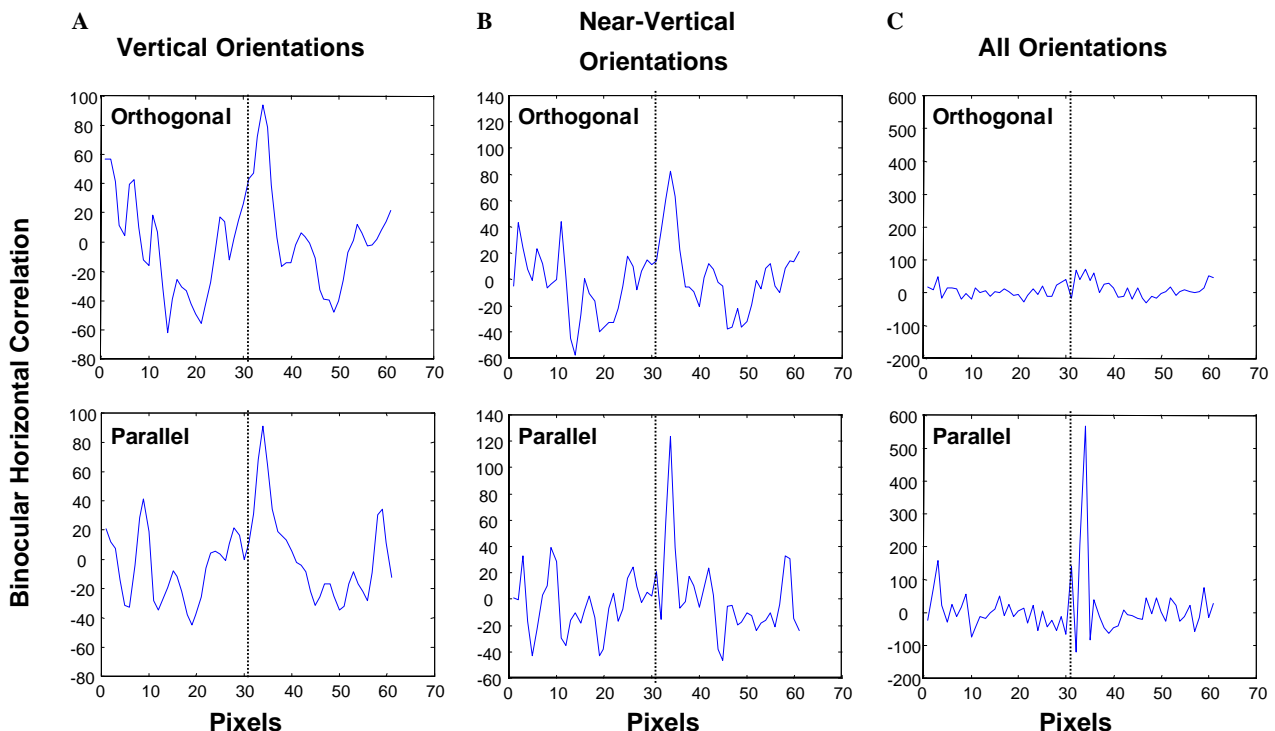We propose potential broad-band models that use vertically and non-vertically oriented SF components

Fig. 4. Horizontal correlation between the 31 × 31-pixel inner squares in the images of the two eyes as a function of the orientation content of the inner squares. The panels in the top (bottom) row show horizontal correlation for stimuli used in the orthogonal-axis (parallel-axis) condition. The mean luminance was removed from all of the images before the computation of horizontal correlation. In the left column (A), the correlations computed from images that were filtered to contain only vertical orientations are nearly identical for the orthogonal- and parallel-axis conditions. In the middle column (B), similar correlations are still obtained in the orthogonal- and parallel-axis conditions when the images contained all orientations within ±15 deg from vertical. In the right column (C), the correlation computed from images that contained all the orientations is substantially higher in the parallel- than in the orthogonal-axes condition. Although disguised by the change in y-axis scale, the correlation in the parallel condition is also higher than in columns (A) and (B). The horizontal disparity between the inner squares of the images used to compute the correlation in this figure was 5.3 arc min. Each pixel on the x-axis is 2 arc min. The vertical dotted line in each panel represents zero disparity.

in the stimulus to compute the horizontal inter-ocular correlation (Fig. 5). Neurons tuned to spatial phase disparities have been found in the visual cortex of monkeys and cats (e.g., Anzai et al., 1997; Ohzawa et al., 1990). These binocular phase-sensitive neurons display preferred orientations that are distributed uniformly between horizontal and vertical (Anzai et al., 1997), and therefore represent the neural basis for our model[s] in which the disparity signals from various orientations are pooled. The general scheme of pooling across neurons with different orientation and spatial frequency

tuning is illustrated in Fig. 5A. This pooling scheme was chosen because it qualitatively mimics a one-dimensional horizontal image correlator, similar to the one used to determine the disparity energy in Fig. 4. Another reason for this choice is that, for any broad-band textured stimulus that contains a horizontal position disparity, as shown in Fig. 1, the distribution of equal phase disparities corresponds to vertical lines in the Fourier domain, which is the direction of pooling that is illustrated in Fig. 5A. A simple learning rule in which neurons that fire similarly cooperate, would be sufficient
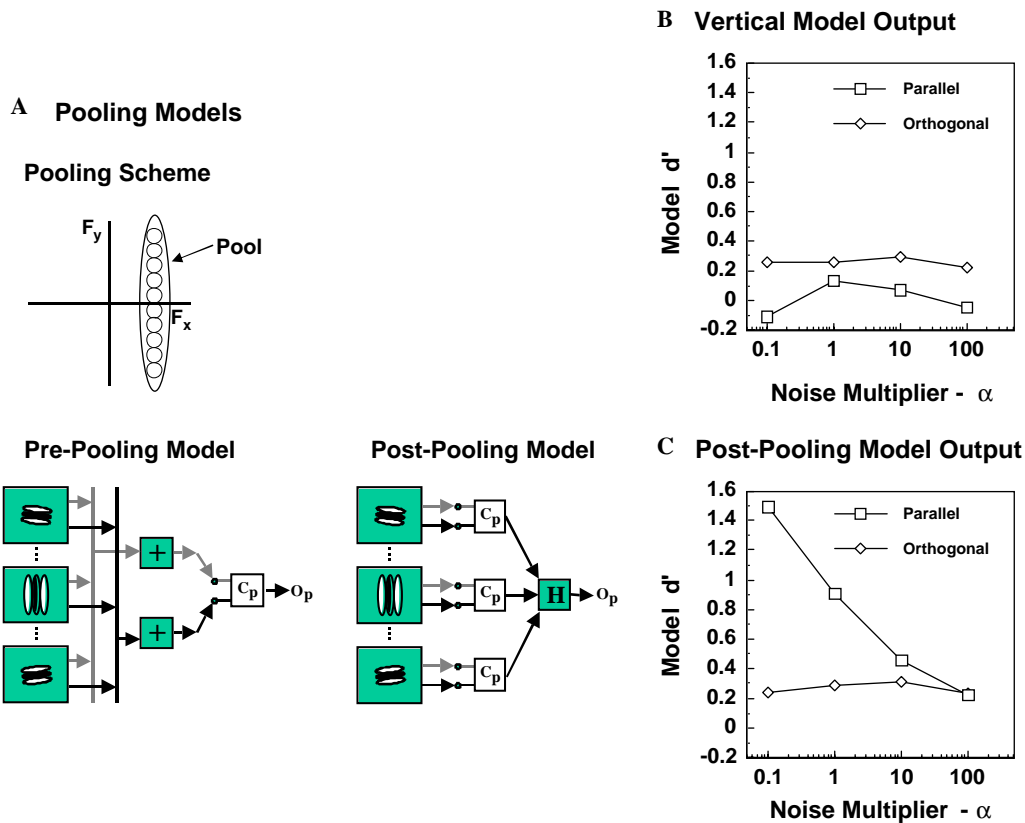

Fig. 5. Broad-band models for the computation of horizontal disparity and comparison of model responses for stimuli used in our experiments. (A) The proposed pre-pooling and post-pooling broad-band models of disparity computations. This panel consists of three sub panels. In the sub-panel labeled *pooling scheme*, the proposed rule for combining signals across various orientations and SFs is illustrated. Each circle in the two-dimensional Fourier plane (F_x, F_y) depicts a quadrature pair of orientation and SF tuned binocular simple cells (see simulation method in Appendix A for details). Both simple cells in a quadrature pair have the same preferred orientation and SF. The angle between the line that joins the origin and the center of each circle and the vertical axis represents the preferred orientation of the quadrature pair. The vertical line that joins the centers of all the circles represents the "horizontal component" of each pair's preferred SF. This common "horizontal component" is defined as the *primary SF*. In the sub-panel labeled *pre-pooling model*, for simplicity, circuitry is illustrated for only a single preferred phase disparity, p, where $p = 2\phi + 90$. The model consists of several simple-cell pairs with preferred orientations ranging from 5 to 175 deg from vertical. Each box with the receptive field icon represents a pair of simple cells. Notice that the preferred SF of each simple cell increases as the preferred orientation changes from vertical to near horizontal, to keep the "horizontal component" of the SF constant and equal to the primary SF. In the pre-pooling model, the responses of simple cell pairs tuned to various orientations are pooled prior to becoming inputs for a complex cell with preferred phase disparity p. In the *post-pooling model*, the output of the simple cell pairs are not pooled, and instead the responses of complex cells with preferred phase disparity, p, and tuned to various orientations are summed by a hyper-complex cell prior to conversion to the final horizontal disparity. In both models, the input to the simple cell pairs is derived from orientation- and spatial frequency-tuned monocular filters. (B) d' as a function of neuronal noise level in the vertical model, which is characterized by a multiplier α (see appendix for definition of α), for stimuli used in 1.5 D parallel (45/45) and orthogonal (45/135) conditions. A larger value of α represents larger internal neural noise. The appendix provides details about how model d' is calculated. The disparity in the stimuli for the parallel (orthogonal) simulation condition was 27 (160) arc sec. In (B) and (C), these disparities represented stereothresholds averaged across observers in the corresponding conditions. (C) d' as a function of neuronal noise level in the post-pooling model, for the same stimuli that were used in (B).
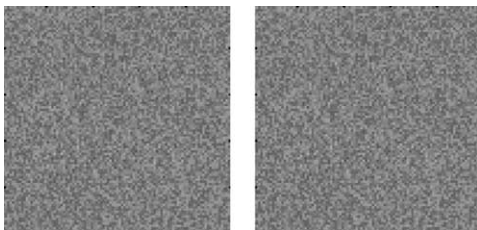
to develop this proposed scheme of neural pooling in the brain.

We considered two specific strategies for pooling disparity energy across orientation and spatial frequency. In the pre-pooling broad-band model, the outputs of simple cells tuned to various orientations and spatial frequencies in a phase-based disparity-energy model (Ohzawa et al., 1990; Qian & Zhu, 1997) were added prior to sending the summed signals to complex cells. In the post-pooling broad-band model, the outputs of the complex cells tuned to various orientations and spatial

A Test Stimulus

B Model Simulations

| Vert | Pre | Post |

frequencies in the phase-based disparity-energy model were summed by a hyper-complex cell prior to the computation of horizontal disparity. As pointed out by an anonymous reviewer, the pre-pooling model is less plausible physiologically because pre-pooling would require that complex cells are isotropic, which they are generally not (e.g., Smith et al., 1997).

We tested the performance of the vertical and post-pooling broad-band models illustrated in Fig. 5A with stimuli used in our present experiments. Details about the implementation of these models is provided in the Appendix A. Although the pre-pooling model was not tested with the stimuli used in our experiments, due to the long time required to run simulations, it was tested with suprathreshold stimuli as described in the following paragraphs. To simulate the models with inputs that yield stereothresholds, we included additive noise at the output of all the neurons in the model. However, a difficulty with this approach is that, a priori, the level of noise that has to be added to each model cell is unknown. Therefore, our approach to test which model better accounts for our experimental data was as follows (see Appendix A for further details): We created one pair of images (left and right eyes) for the (45, 45) parallel-axis condition and another pair of images for the (45,135) orthogonal-axes condition. The horizontal disparity between the images in each pair of stimuli was set to the empirically determined stereothreshold, averaged across observers, for each condition. Using these two images pairs, we simulated the vertical and post-pooling models with various levels of added noise. For each noise level, the model simulation was run five times, which represents a tradeoff between the requirement to average the results across runs and the duration of a single simulation run. The output of each simulation run was a disparity map; these maps were averaged across
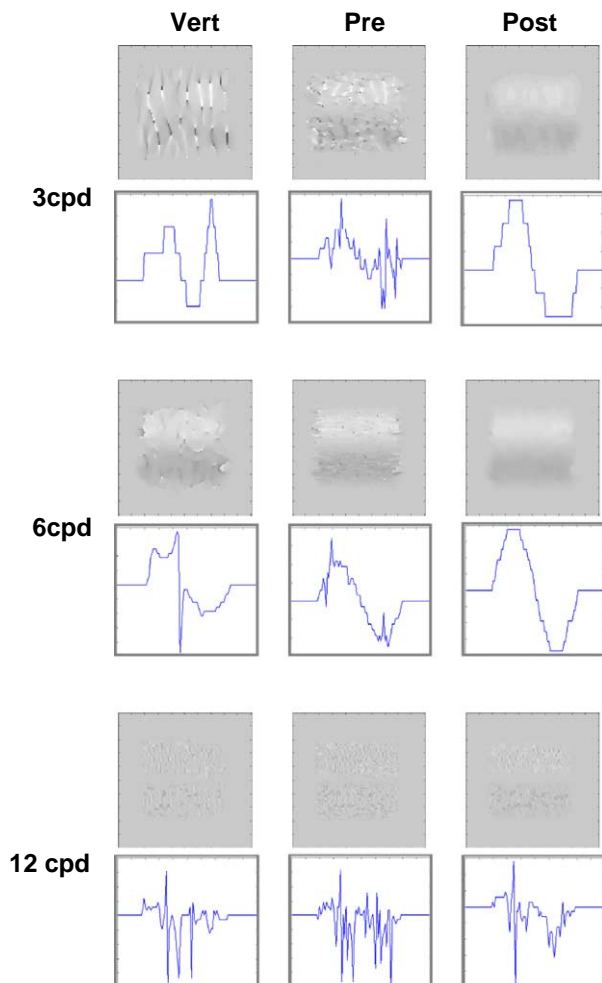
Fig. 6(A) The binocular stimulus used for comparing the two broad-band pooling models to the vertical model. When fusion is achieved, observers should see one cycle of sinusoidal depth modulation in the vertical direction. If viewed from a distance where the total size of each image is 3.3 deg, the peak disparity of the sinusoidal modulation is 2 arc min. (B) Each gray image is a spatial representation of the horizontal disparities (disparity map) computed by the model labeled at the top of the column using the stimulus shown in (A). The magnitude and sign of the disparity in the inner rectangle are represented by the luminance contrast: positive contrast represents uncrossed and negative contrast represents crossed disparities in the cross-fused stimulus. The plot below each disparity map represents the horizontal disparity values at spatial locations along a vertical line passing through the middle of the disparity map and is ideally expected to be a sinusoidal waveform. The first, second and third columns show simulation results for the vertical, pre-pooling and post-pooling models, respectively. The orientation- and SF-tuned simple and complex cells were modeled by modifying the formulations of Qian and Zhu (see simulation methods in Appendix A for details). Details of the circuitry for simple and complex cells can be found in Qian and Zhu's original (1997) paper. Simulations were performed for primary spatial frequencies of 3, 6 and 12 cpd.

the five simulations for each combination of stimuli and model noise. The averaged disparity maps were analyzed to obtain values of d', which represents the discriminability between the distribution of disparity values in the inner 31×31 pixel square and those in a 31×31-pixel square region in the outer frame of each map. We claim that if the inputs used for the simulation are stereothresholds, and if the model is valid, then for some critical noise level the calculated d' for the parallel-axis and the orthogonal-axes conditions should be equal. Expressed graphically, if d' is plotted as a function of the model noise then the curves for the parallel-axis and orthogonal-axes conditions should intersect at some noise level.

The results of these simulations for the vertical and post-pooling models are shown in Figs. 5B and C. Notice that the plots of d' for the parallel-axis and orthogonal-axes conditions intersect for the post-pooling model but not for the vertical model. Also note that the d' values determined in parallel-axis condition for the vertical model are negative for some noise levels, indicating that the model's aggregate disparity for the inner square is reversed in sign. Finally, the d' values determined for the vertical model in the parallel-axis condition are lower than those in the orthogonal-axes condition for the entire range of tested noise levels. These simulation results contradict our experimental finding that the stereothreshold is lower in the parallel-axis compared to orthogonal-axes condition. Taken together, the outcomes of these simulations indicate that the post-pooling model, but not the vertical model, can account for the empirical data reported in this paper.

The d' values that are plotted in Figs. 5B and C for the post-pooling model are not close to unity at the critical noise level. This is because only five disparity maps were averaged for each noise level; averaging a larger number of maps should reduce the disparity noise in the average map and increase the values of d' substantially. Although more averaging of disparity maps would also be expected to improve the performance of the vertical model, it is unlikely that the results for this model would change qualitatively to become more consistent with our data.

We hypothesize that pooling across orientation-tuned disparity mechanisms should enhance the lateral spatial resolution of the stereovision system. To evaluate this hypothesis, we tested the performance of the vertical and broad-band models with the spatially modulated suprathreshold disparity stimuli shown in Figs. 6A and 7A (for detailed simulation methods please see Appendix A). In Figs. 6B and 7B, the performance of both of the pooling models is compared with that of the vertical model. (Note that the vertical model is tested only for comparison and not as a viable model for stereopsis because it fails to account for the principal aspects of the

A　Stimulus
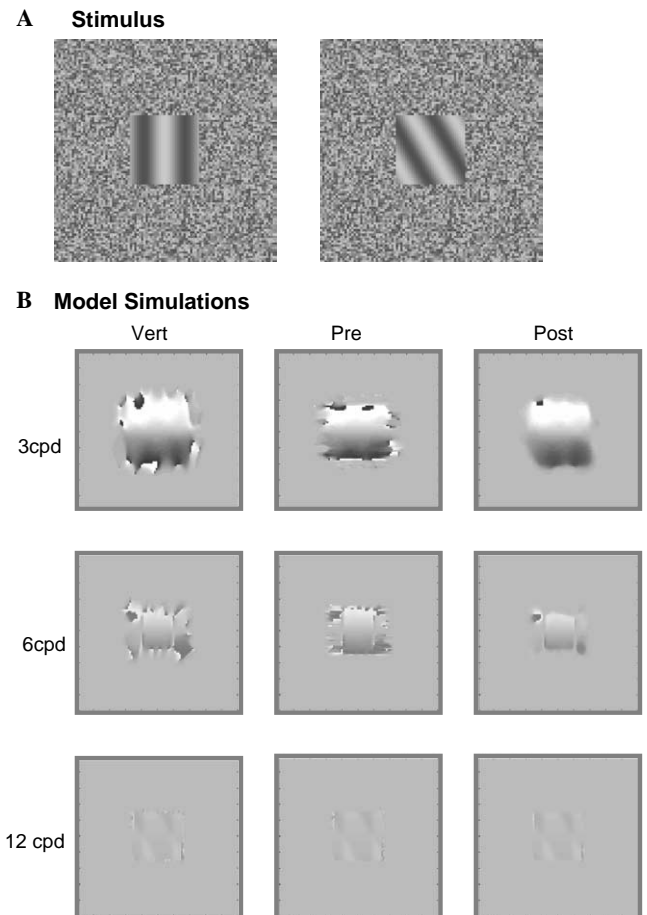

B　Model Simulations

Fig. 7. Comparison of model responses for a binocular stimulus consisting of spatial frequency gratings at different orientations in the two eyes. (A) Gratings of different orientations and SF in the inner squares of the images presented to the two eyes. The outer frame in both the images consists of correlated random-dots with no disparity. The SF of the oriented grating is such that the *horizontal* luminance modulations have the same spatial frequency in the two eyes. Upon fusion, observers should see a slanted surface with depth changing from behind to in-front of the outer frame (or vice-versa) as a function of the vertical distance from the top of the inner square. Despite minimal overlap in the SF and orientation content of the images in the two eyes, a robust perception of depth is obtained from the stimulus. (B). The disparity maps obtained for the stimulus in (A) using the vertical, pre- and post-pooling models of disparity computation. The models were simulated for primary SFs of 3, 6, and 12 cpd. For observers who could fuse the stimulus, the perceived depth of the inclined plane is predicted most closely by the disparity map from the post-pooling model that corresponds to a primary SF of 3 cpd. Both the pre- and post-pooling models suggest that the robust perception of slant arises as a result of pooling disparity signals from various orientation- and SF-tuned disparity neurons.

data in Fig. 3) Although all three models can detect the disparity modulations to some extent, the broad-band models perform substantially better than the vertical model in encoding a spatially changing disparity. It is also clear that the post-pooling model is more robust than the pre-pooling model in encoding the sinusoidal disparity modulation at spatial scales corresponding to 3 and 6 cpd. This means that a further enhancement in

disparity estimation may be possible if disparity information is combined subsequently across spatial scales. Because the post-pooling model is more robust, we favor this broad-band model over the pre-pooling model and suggest that the functional site of orientation pooling is beyond the binocular complex cells.

The results of this study are consistent with our previous conclusion (Patel et al., 2003b) that oblique retinal image disparities carry a substantial proportion of the information about stereoscopic depth that is used by the human visual system. The data suggest that the horizontal inter-ocular correlator (Banks, Gepshtein, & Landy, 2004; Cormack, Stevenson, & Schor, 1991) that computes horizontal image disparity should use the disparity signals from non-vertically as well as from vertically tuned neurons. By pooling signals from a large number of obliquely tuned binocular neurons, the stereovision system can encode spatial changes in horizontal disparity with high signal-to-noise ratio (Fleet, Wagner, & Heeger, 1996; Patel et al., 2003b) and improved spatial resolution. The physiologically plausible post-pooling model proposed in this paper clarifies how disparity-tuned neurons in V1, which have spatially extended receptive fields, can account for the perceived depth of a surface that has steep variations in depth (Mahew & Frisby, 1979). Along-with a recent study by Nienborg, Bridge, Parker, and Cumming (2004), this model suggests that the site at which changes in horizontal disparities are encoded may be beyond V1, perhaps in area V2 or MT. Because a spatio-temporal correlator is required to analyze visual motion signals as well, we hypothesize that pooling signals from motion mechanisms tuned to non-primary as well as to the primary direction of stimulus motion could similarly enhance the spatial resolution of the visual motion system, i.e., its ability to encode spatially changing visual motion signals.

Acknowledgments

Appendix A. Simulation method

The energy model of Qian and Zhu (1997) was extended to generate the various models used in this study. Details of the original model can be found in Qian and Zhu's, 1997 paper and in Patel et al. (2003b). Briefly, the generic module in Qian's and Zhu's

model is shown in the panel labeled OF module in Fig. 8.

In the complete model, a bank of OF modules extracts the disparity energy at each location in the (fused) retinal image. Each bank contains OF modules tuned to a range of SFs, orientations, and phase disparities. The pattern of connections between the OF modules in a bank distinguishes the pre-pooling and the post-pooling models that are described in this paper.

A.1. Pre-pooling model

In this model, one complex cell receives signals that are pooled from various orientation and SF tuned quadrature pairs of simple cells at each spatial location and value of phase disparity, (Fig. 5A). The quadrature pairs of simple cells that form a pool have a definite relationship between preferred orientation and preferred SF. For a given preferred orientation, the "horizontal component" of the preferred SF is equal to the *primary* SF (see Fig. 5A) of the pool. The primary SF, which also characterizes the pool, is defined to be equal to the preferred SF of the cell in the pool whose preferred orientation is *vertical*. For each preferred phase disparity and primary SF, the model includes 19 quadrature-pair simple cells with preferred orientations spaced equally
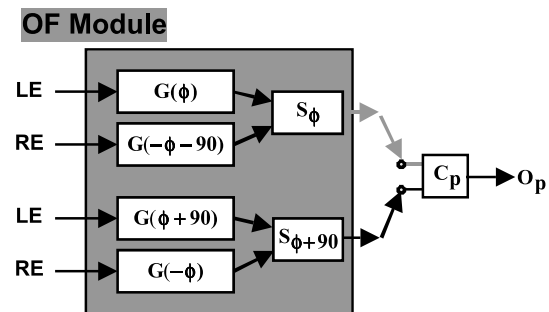

Fig. 8. Schematic of the elementary module in Qian and Zhu's implementation of the disparity-energy model. The OF module consists of four monocular cells, two binocular simple cells and one binocular complex cell. The binocular cell's orientation, SF and phase disparity tuning properties are derived from the antecedent monocular cells. Each module has a preferred orientation, SF and phase disparity. Each simple cell receives input from two monocular filters, one from each eye. The receptive field of each monocular filter is modeled as an oriented Gabor function (G). The space-constant of the circularly symmetric Gaussian envelope of G was equal to half the spatial period of the oriented carrier grating. G was defined within a square matrix of dimension corresponding to six times the space-constant of the Gaussian envelope. The monocular filters for one simple cell (S_ϕ) have the sum of spatial phases (LE + RE) of −90 pdeg while those for the other simple cell ($S_{\phi+90}$) have the sum of spatial phases as 90 pdeg. Further, for each eye, the absolute difference between the spatial phase of the monocular filters is 90 pdeg. Together, the two simple cells connected in this configuration form a linear quadrature pair. A complex cell (C_p) sums the rectified signals from the two simple cells to produce the output O_p of the OF module. The preferred phase disparity (p) of a OF module is determined by the phase parameter (ϕ) of the Gabor functions and is equal to 2ϕ.

between 5 and 175 deg (orientation resolution of 10 odeg, where 90 odeg represents vertical orientation). For each primary SF (e.g., 3 cpd), the preferred SF for the 19 quadrature pairs of cells was a function of preferred orientation (preferred SF = primary SF/sin(preferred orientation)) and ranged from approximately 3 to 34 cpd. For each primary SF, 80 phase-disparity tuned complex cells with preferred phase disparities are spaced equally in the range between −180 and 175.5 pdeg (phase disparity resolution of 4.5 pdeg). For each preferred phase disparity, the output of all 19 quadrature pairs of simple cells are added as shown in Fig. 5A and the summed signals are sent to a complex cell. The phase disparity preferred by the most active of the 80 complex cells is finally converted to horizontal disparity, according to the primary SF of the pool. Identical computations are performed for each spatial location in the input retinal image. The final output of the model is a two-dimensional representation of horizontal disparity (e.g., Fig. 6B), corresponding to the (fused) two-dimensional retinal image. This 2-D representation of disparities is called a disparity map. Note that Qian and Zhu (1997) applied a low-pass disparity filter to the disparity maps obtained from the responses of the model neurons. In Figs. 6B and 7B, we show the unfiltered disparity maps. We simulated the model for primary SFs of 3, 6, and 12 cpd. Because the pooling of disparity signals in this model occurs prior to the non-linear operation of rectification, this pooling scheme is linear.

A.2. Post-pooling model

For each spatial location and value of single phase disparity tuning, this model consists of a bank of complete OF modules, each with a different orientation and SF preference. The model includes 19 OF modules with preferred orientations spaced equally between 5 and 175 odeg, for each preferred phase disparity and primary SF. A hyper-complex cell pools the output of the 19 OF modules for each phase disparity (Fig. 5A). The preferred phase disparity of the hyper complex cell is the same as its 19 input OF modules. The model uses 80 phase-disparity tuned hyper complex cells with preferred phase disparities spaced equally in the range between −180 and 175.5 pdeg for each primary SF. The preferred phase disparity of the most active of the 80 hyper complex cells is finally converted to a horizontal disparity, based on the primary SF of the pool. These computations are performed for each spatial location in the fused retinal image. The final output of the model is a two-dimensional representation of horizontal disparities (e.g., Fig. 6B) corresponding to the two-dimensional retinal images. We simulated the model for primary SFs of 3, 6, and 12 cpd. Because pooling in this model occurs after the non-linear operation of rectification, this pooling scheme is non-linear.

A.3. Vertical model

For each spatial location and value of single phase disparity tuning, this model consists of just one OF module tuned to a vertical orientation at a given SF. For each SF, the model uses 80 phase-disparity tuned complex cells with preferred phase disparities spaced equally in the range between −180 and 175.5 pdeg. The preferred phase disparity of the most active of the 80 complex cells is finally converted to a horizontal disparity, based on the given SF. These computations are performed for each spatial location in the fused retinal image. The final output of the model is a two-dimensional representation of horizontal disparities (e.g., Fig. 6B) corresponding to the two-dimensional retinal images. We simulated the model for SFs of 3, 6, and 12 cpd.

A.4. Noise in the model

To properly simulate the models with inputs that yield stereothresholds, we included additive noise at the output of all the neurons in the models. Due to time constraints, we only tested the vertical and the post-pooling models. We assumed that the additive noise added to the output of each cell, which represented firing rate noise, was uniformly distributed. The peak-to-peak range of noise was different for each type of cell. The noise range for all the monocular filters was symmetric and bi-polar (-25α to 25α) while that for the rest of the cells was unipolar. The noise range for all the simple and complex cells was $0–\alpha$ and $0–0.1\alpha$, respectively. For the post-pooling model, the noise range for all the hyper-complex cells was 0 to 0.1α. The noise in the model was uncorrelated across all the neurons regardless of the spatial location they represent.

Both of the models were in all other ways identical to those described in the above sections. Both models were simulated with two inputs: (1) 45,45 1.5 D parallel-axis condition stimulus with 27 arc sec disparity and (2) 45,135 1.5 D orthogonal-axis condition with 160 arc sec disparity. The values, 27 and 160 arc sec correspond to the stereothreshold averaged across observers in the parallel and the orthogonal conditions, respectively (see Fig. 3A). Both models were simulated with these inputs for different values of α ranging from 0.1 to 100. For each α and input the models were simulated five times, yielding five disparity maps which were averaged for further analysis. Consequently, for each α, there were finally four averaged disparity maps (two inputs × two models).

From each averaged disparity map, d' was computed. A histogram of disparity values corresponding to the 31×31 inner square was computed in bins of 0.01 arc-min. Another similar histogram of disparity values representing the outer frame was also computed. For the outer-frame's histogram, a 31×31 square patch of pixels to the left of the inner square was used. From each

histogram, the first (equivalent to mean) and second (equivalent to standard-deviation) order moments were computed. Let $\mu_c(\mu_o)$ and $\sigma_c(\sigma_o)$ represent the first and the second order moments for the inner (outer) square (frame). Then,

$$d' = \frac{2(\mu_c - \mu_o)}{\sigma_c + \sigma_o}.$$

References

Akutsu, H., Bedell, H. E., & Patel, S. S. (2000). Recognition thresholds for letter with simulated dioptric blur. *Optometry and Vision Science, 77*, 524–530.

Anzai, A., Ohzawa, I., & Freeman, R. D. (1997). Neural mechanisms underlying binocular fusion and stereopsis: Position vs. phase. *Proceedings of the National Academy of Sciences of the United States of America, 94*, 5438–5443.

Banks, M. S., Gepshtein, S., & Landy, M. S. (2004). Why is spatial stereoresolution so low? *Journal of Neuroscience, 24*, 2077–2089.

Barlow, H. B., Blakemore, C., & Pettigrew, J. D. (1967). The neural mechanism of binocular depth discrimination. *Journal of Physiology, 193*, 327–342.

Blake, R., Camisa, J. M., & Antoinetti, D. N. (1976). Binocular depth discrimination depends on orientation. *Perception & Psychophysics, 20*, 113–118.

Chen, S. I., Hove, M., McCloskey, C. L., & Kaye, S. B. (2005). The effect of monocularly and binocularly induced astigmatic blur on depth discrimination is orientation dependent. *Optometry and Vision Science, 82*, 101–113s.

Chino, Y. M., Smith, E. L., Hatta, S., & Cheng, H. (1997). Postnatal development of binocular disparity sensitivity in neurons of the primary visual cortex. *Journal of Neuroscience, 17*, 296–307.

Cormack, L. K., Stevenson, S. B., & Schor, C. M. (1991). Interocular correlation, luminance contrast and cyclopean processing. *Vision Research, 31*, 2195–2207.

Cormack, L. K., Stevenson, S. B., & Landers, D. D. (1997). Interactions of spatial frequency and unequal monocular contrasts in stereopsis. *Perception, 26*, 1121–1136.

Farell, B. (1998). Two-dimensional matches from one-dimensional stimulus components in human stereopsis. *Nature, 395*, 689–693.

Felleman, D. J., & Van Essen, D. C. (1987). Receptive field properties of neurons in area V3 of macaque monkey extrastriate cortex. *Journal of Neurophysiology, 57*, 889–920.

Fleet, D. J., Wagner, H., & Heeger, D. J. (1996). Neural encoding of binocular disparity: Energy models, position shifts and phase shifts. *Vision Research, 36*, 1839–1859.

Gonzalez, F., Krause, F., Perez, R., Alonso, J. M., & Acuna, C. (1993). Binocular matching in monkey visual cortex: Single cell responses to correlated and uncorrelated dynamic random dot stereograms. *Neuroscience, 52*, 933–939.

Halpern, D. L., & Blake, R. (1989). How contrast affects stereoacuity. *Perception, 17*, 483–495.

Hess, R. F., Liu, C. H., & Wang, Y. Z. (2003). Differential binocular input and local stereopsis. *Vision Research, 43*, 2303–2313.

Hubel, D. H., & Wiesel, T. N. (1970). Stereoscopic vision in macaque monkey. *Nature, 225*, 41–42.

Legge, G. E., & Gu, Y. (1989). Stereopsis and contrast. *Vision Research, 29*, 989–1004.

Lovasik, J. V., & Szymkiw, M. (1985). Effects of aniseikonia, anisometropia, accommodation, retinal illuminance, and pupil size on stereopsis. *Investigative Ophthalmology & Visual Science, 26*, 741–750.

Mahew, J. E. W., & Frisby, J. P. (1979). Surfaces with steep variations in depth pose difficulties for orientationally tuned disparity filters. *Perception, 8*, 691–698.

Mansfield, J. S., & Parker, A. J. (1993). An orientation-tuned component in the contrast masking of stereopsis. *Vision Research, 33*, 1535–1544.

Maske, R., Yamane, S., & Bishop, P. O. (1986). Stereoscopic mechanisms: Binocular responses of the striate cells of cats. *Proceedings of the Royal Society of London. Series B. Biological Sciences, 229*, 227–256.

Maunsell, J. H. R., & Van Essen, D. C. (1983). Functional properties of neurons in middle temporal visual area of the macaque monkey. II Binocular interactions and sensitivity to binocular disparity. *Journal of Neurophysiology, 49*, 1148–1167.

Morgan, M. J., & Castet, E. (1997). The aperture problem in stereopsis. *Vision Research, 37*, 2737–2744.

Nienborg, H., Bridge, H., Parker, A. J., & Cumming, B. G. (2004). Receptive field size in V1 neurons limits acuity for perceiving disparity modulation. *Journal of Neuroscience, 24*, 2065–2076.

Ohzawa, I., DeAngelis, G. C., & Freeman, R. D. (1990). Stereoscopic depth discrimination in the visual cortex: Neurons ideally suited as disparity detectors. *Science, 249*, 1037–1041.

Patel, S. S., Ukwade, M. T., Bedell, H. E., & Sampath, V. (2003a). Near stereothresholds measured with random-dot stereograms using phase disparities. *Optometry, 74*, 453–461.

Patel, S. S., Ukwade, M. T., Stevenson, S. B., Bedell, H. E., Sampath, V., & Ogmen, H. (2003b). Stereoscopic depth perception from oblique phase disparities. *Vision Research, 43*, 2479–2492.

Poggio, G. F., Motter, B. C., Squatrito, S., & Trotter, Y. (1985). Responses of neurons in visual cortex (V1 and V2) of the alert Macaque to dynamic random-dot stereograms. *Vision Research, 25*, 397–406.

Prince, S. J, Pointon, A. D, Cumming, B. G, & Parker, A. J. (2002). Quantitative analysis of the responses of V1 neurons to horizontal disparity in dynamic random-dot stereograms. *Journal of Neurophysiology, 87*, 191–208.

Qian, N., & Zhu, Y. (1997). Physiological computation of binocular disparity. *Vision Research, 37*, 1811–1827.

Schor, C. M., & Heckmann, T. (1989). Interocular differences in contrast and spatial frequency: Effects on stereopsis and fusion. *Vision Research, 29*, 837–847.

Simons, K. (1984). Effects of stereopsis on monocular vs. binocular degradation of image contrast. *Investigative Ophthalmology & Vision Science, 25*, 987–989.

Simmons, D. R., & Kingdom, F. A. A. (1995). Differences between stereopsis with isoluminant and isochromatic stimuli. *Journal of the Optical Society of America. A, Optics and Image Science, 12*, 2094–2104.

Smith, E. L., III, Chino, Y. M., Ni Jinren Ridder, W. H., III, & Crawford, M. L. J. (1997). Binocular spatial phase tuning characteristics of neurons in the macaque striate cortex. *Journal of Neurophysiology, 78*, 351–365.

Stevenson, S. B., & Cormack, L. K. (2000). A contrast paradox in stereopsis, motion detection and Vernier acuity. *Vision Research, 40*, 2881–2884.

Stevenson, S. B., & Schor, C. M. (1997). Human stereo matching is not restricted to epipolar lines. *Vision Research, 37*, 2717–2723.

van Ee, R., & Anderson, B. L. (2001). Motion direction, speed and orientation in binocular matching. *Nature, 410*, 690–694.

Westheimer, G., & McKee, S. P. (1980). Stereoscopic acuity with defocussed and spatially filtered retinal images. *Journal of the Optical Society of America. A, Optics and Image Sciences, 70*, 772–778.

Wheatstone, C. (1838). Contributions to the physiology of vision - Part the first. On some remarkable, and hitherto unobserved, phenomena of binocular vision. *Philosophical Transactions of the Royal Society of London. Series B, Biological Sciences, 2*, 371–393.

Wood, I. C. J. (1983). Stereopsis with spatially degraded images. *Opthalmic and Physiological Optics, 3*, 337–340.